JACS
JOURNAL OF THE AMERICAN CHEMICAL SOCIETY

Article

Asymmetric Hydroboration of Heteroaryl Ketones by Aluminum Catalysis

Yury N. Lebedev, Iuliia Polishchuk, Bholanath Maity, Luigi Cavallo, and Magnus Rueping

J. Am. Chem. Soc., **Just Accepted Manuscript** • DOI: 10.1021/jacs.9b10364 • Publication Date (Web): 08 Nov 2019

is published by the American Chemical Society. 1155 Sixteenth Street N.W., Washington, DC 20036

Asymmetric Hydroboration of Heteroaryl Ketones by Aluminum Catalysis

Yury Lebedev,[a,b*] Iuliia Polishchuk,[a,b] Bholanath Maity,[a*] Luigi Cavallo,[a*] Magnus Rueping[a,b*]

[a] King Abdullah University of Science and Technology (KAUST) KAUST Catalysis Center (KCC) Thuwal, 23955-6900 (Saudi Arabia)

[b] Institute of Organic Chemistry, RWTH Aachen University, Landoltweg 1, 52074 Aachen (Germany)

KEYWORDS: asymmetric hydroboration, aluminum catalysis, chiral heteroaromatic alcohols, DFT

ABSTRACT: A series of methyl aluminum complexes bearing chiral biphenol-type ligands were found to be highly active catalysts in the asymmetric reduction of heterocyclic ketones (S/C = 100 – 500, ee up to 99%). The protocol is suitable for a wide range of substrates and has a high tolerance to functional groups. The formed 2-heterocyclic-alcohols are valuable building blocks in drug discovery or can be used as ligands in asymmetric catalysis. Isolation and comprehensive characterization of the reaction intermediates support a catalysis cycle proposed by DFT calculations.

■ INTRODUCTION

Chiral 2-pyridine alcohols and related heterocyclic compounds are valuable structural units in the pharmaceutical and agrochemical industries[1] as well as important ligands in transition metal catalysis.[2] For example, 7-(1-pyrindanyl)propargyl ether[1h] is a rasagiline analogue and carbinoxamine and bepotastine besilate are useful histamine H1 antagonists (Figure 1).[3] Furthermore, reaction with amines allows a ready access to the corresponding chiral amines with the inversion of configuration.[4] Access to this class of compounds is provided via bio-enzymatic[5] as well as organo-[6] and transition metal catalyzed enantioselective reductions.[7] Despite the significant progress achieved several drawbacks including the relatively high catalyst loading, the necessity to protect the nitrogen atom or narrow substrate scope usually limited to *ortho*-substituted aryl groups, must be considered. Hence, the development of improved protocols for the challenging highly asymmetric catalytic reduction of 2-pyridine ketones and analogues is desirable. Although significant progress has been achieved in substitution of transition metal catalysts by their main group congeners, the highly enantioselective reduction of C=X (X = O, NR, CR_2) bonds remains relatively scarce.[8] In the last few years considerable attention was devoted to aluminum hydride and alkyl complexes[9] as they were found to be highly active catalysts in the hydrosilylation and hydroboration of aldehydes and ketones.[10] The latter findings prompted us to develop an Al-based catalyst for the asymmetric reduction of ketones.

Herein, we report a highly enantioselective protocol for the hydroboration of a wide range of 2-pyridine and analogous heterocyclic ketones utilizing a low loading of a well-defined aluminum catalyst.

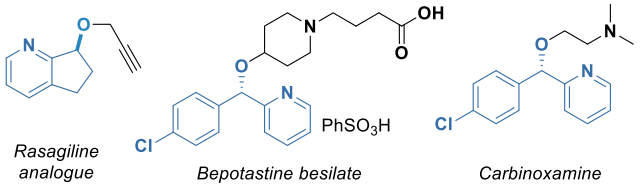

Figure 1. Bioactive compounds containing 2-pyridine alcohol structural fragment.

■ RESULTS AND DISCUSSION

Initially we tested a number of aluminum complexes generated *in situ* by reacting stoichiometric amounts of $AlMe_3$ and commercially available chiral diols (Table 1). Toluene was the solvent of choice due to its non-coordinating nature and good solubilizing properties for all components. As shown in Table 1, the effect of the ligand on the conversion of the ketone **1a** to alcohol **3a** and asymmetric induction was significant. The relatively unhindered BINOL and TADDOL as well as the hindered $SiPh_3$-BINOL (entries 1–3) resulted in poor to moderate performance of the catalytic system. In contrast, moderately bulky VANOL, VAPOL and CF_3-BINOL showed superior results (entries 4-6). (R)-CF_3-BINOL was selected for further development as it provided excellent *ee*. Furthermore, the flanking substituents of the BINOL scaffold can be easily tuned to adjust the reactivity and selectivity for different substrates. Screening of solvents confirmed toluene to provide the highest performance for the catalyst (SI, Table S5). It is important to note that HBPin was the borane of choice and another commonly utilized catecholborane, gave only racemic products with good conversion. Furthermore, for 9-BBN no product was detected (SI, Table S1).

Table 1. Ligand screening for the aluminum catalyzed asymmetric hydroboration of 2-acetylpyridine.

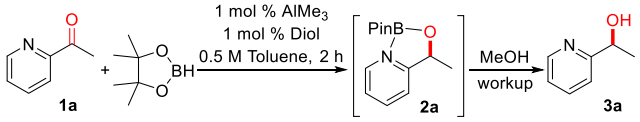

Entry	Ligand	Conversion	*ee* (%)
1	(R)-BINOL	>36	80 (*R*)
2	(R,R)-TADDOL	43	60 (*R*)
3	(R)-$SiPh_3$-BINOL	28	10 (*R*)
4	(S)-VANOL	98	98 (*S*)
5	(R)-VAPOL	99	98 (*R*)
6	(R)-CF_3-BINOL	99	98 (*R*)

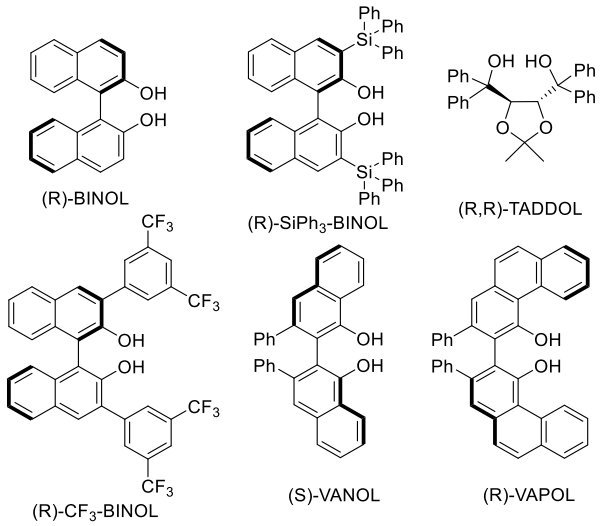

Reaction conditions: **1a** (1 mmol), toluene (1.5 mL), HBPin (1.05 mmol), 1 mol % Al-catalyst (0.01 mmol $AlMe_3$ + 0.01 mmol ligand in 0.5 mL of toluene). Conversion was determined by GC after hydrolysis, *ee* was determined by HPLC analysis using a chiral stationary phase.

Under the optimized reaction conditions, we extended the substrate scope to different 2-pyridine ketones as well as pyrazine, imidazole and thiazole derivatives **1a-z** (Table 2). To our delight the reaction was found to be highly tolerant to a variety of aryl and alkyl substituents, functional groups, cyclic substrates and additional donor atoms. The hydroboration was performed on a 4 mmol scale with 1 M concentration of the substrate. For 2-acetylpyridine (**1a**), the protocol was scaled up to 10 mmol using 0.2 mol % catalyst loading without loss of yield and ee (96%, 98% *ee*).

Stereochemical analysis of the isolated α-methyl-2-pyridinemethanol (**3a**) was performed by comparing its optical rotation and retention time on a chiral stationary phase with those of commercial (R)-α-methyl-2-pyridinemethanol demonstrating that (R)-configured CF_3-BINOL provides the (R)-configurated product.

Table 2. Asymmetric Al – catalyzed hydroboration of ketones.

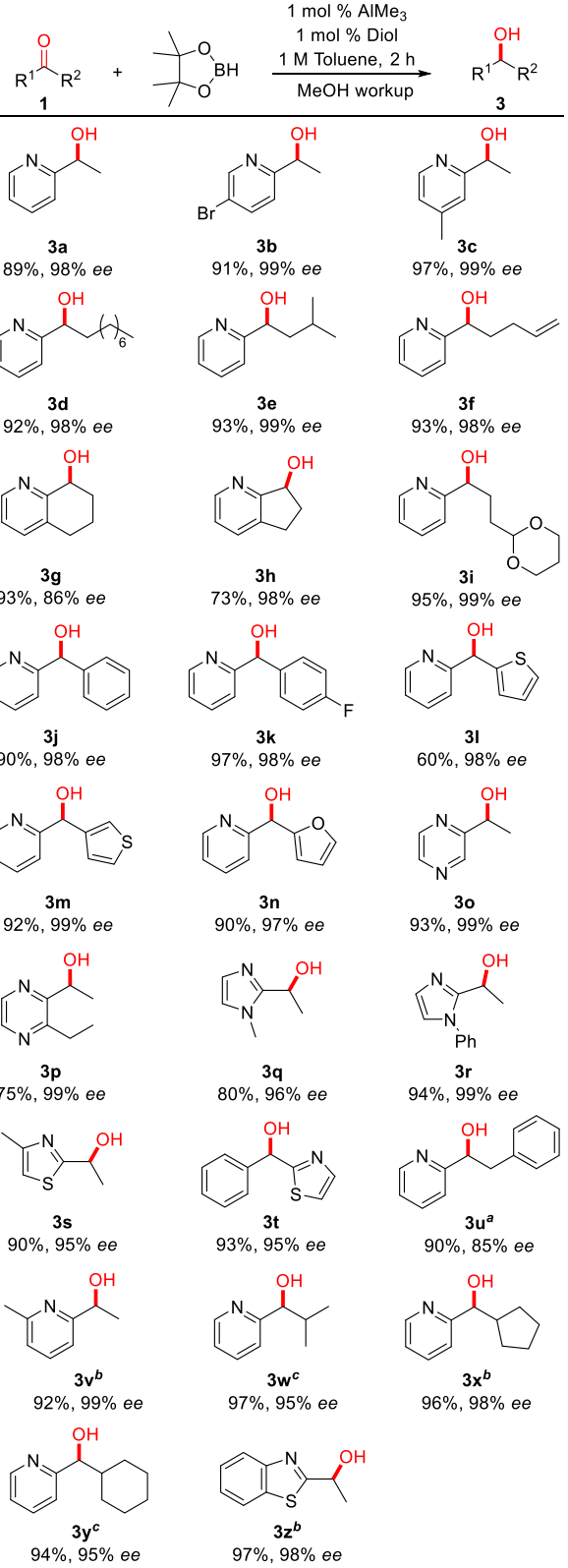

Reaction conditions: **1** (4 mmol), 4.05 mmol HBPin, 1 mol % catalyst (0.04 mmol $AlMe_3$ + 0.04 mmol (R)-CF_3-BINOL), 1 M

toluene concentration, ambient temperature, 2 h. [(a)](R)-BINOL was used. [(b)](R)-VAPOL was used. [(c)](S)-VANOL was used.

Although 2-acethyl-5-methyl thiazole (**1s**) afforded very high yield and ee for the corresponding alcohol **3s**, the performance of the catalyst bearing the CF_3-BINOL ligand was found to be sensitive to ortho- substitution in the heterocyclic ring and bulky alkyl groups at the carbonyl position. Nevertheless, switching to (R)-BINOL, (S)-VANOL or (R)-VAPOL provided excellent yields and ee's for the isolated alcohols **3u-3z**. However, the screening of ligands and solvents for acetophenone and several imines did not allow to achieve a similar performance (SI, Tables S2 -S3).

Characterization of the catalyst and mechanistic considerations

To gain an insight into the mechanism we first tested if an adduct between HBPin and 2-acethylpyridine (**1a**) forms in aromatic solvents. In the ^{1}H, ^{13}C and ^{11}B NMR spectra (benzene-d_6), the positions of the peaks of an equimolar 0.25 M mixture were identical to those of the individual compounds, indicating that no complexation occurred in solution. Also no significant product formation was achieved and traces of product were observed after stirring the reaction for 10 days at ambient temperature.

Next, adduct **2a** isolated from the reaction of **1a** with HBPin in the presence of [(R)-CF_3-BINOL-AlMe]$_2$ was subjected to single crystal XRD analysis, rendering the (R) configuration of the product (Figure 2). The boron center coordinates to the pyridine nitrogen atom with the B-N bond (1.633(3) Å) slightly longer than the sum of single bond covalent radii of the elements (1.56 Å)[11] and falls in the range of B-N distances (1.655(3) – 1.611(3) Å) in previously characterized Py-B(OAr)$_3$ adducts.[12] The N-B-O1 angle (98.0(2)°) is distorted from the ideal sp^3-hybridized one.

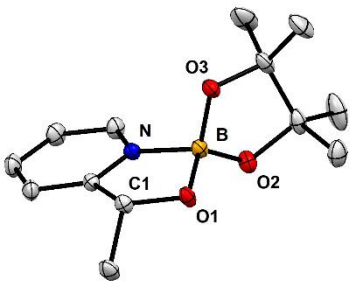

Figure 2. MERCURY plot of the molecular structure of **2a**. Hydrogen atoms are omitted for clarity. Selected bond lengths [Å] and angles [°]: N-B 1.633(3), O1-B 1.468(3), O2-B 1.431(3), O3-B 1.435(3), C1-O1 1.401(3). N-B-O1 98.0(2), O2-B-O3 107.7(2).

Suitable single crystals of the *in situ* generated catalyst were obtained upon cooling an *n*-hexane solution to –35 °C and their XRD analysis showed a dimer [(*R*)-CF_3-BINOL-AlMe]$_2$ formed via oxygen bridges (Figure 3). The dimeric structure is presumably retained in solution, as indicated by the three signals in a 12:6:6 ratio for the CF_3 groups in the ^{19}F NMR spectrum in benzene-d_6 (SI, Figure S9).

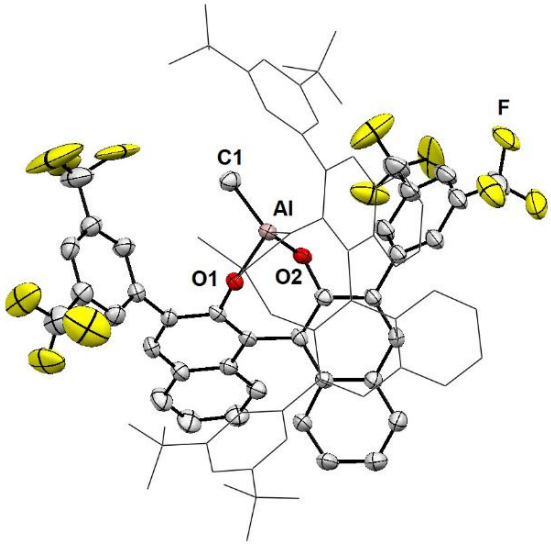

Figure 3. MERCURY plot of the molecular structure of [(R)-CF_3-BINOL-AlMe]$_2$. Hydrogen atoms are omitted for clarity. Selected bond lengths [Å]: Al1-O1 1.856(3), Al1-O2 1.855(3), Al1-C1 1.896(3).

In a subsequent experiment, 0.5 equiv. of *in situ* generated [(R)-CF_3-BINOL-AlMe]$_2$ was added dropwise to 4 equiv. 2-acethylpyridine in *n*-hexane. A voluminous precipitate formation was observed thereby. The filtrate was determined to contain only 2 equivalents of the unreacted ketone. The ^{1}H, ^{13}C, ^{19}F NMR spectra in benzene-d_6 of the isolated solid amorphous material were inconclusive, and, upon hydrolysis on silica, (R)-CF_3-BINOL was recovered. This result can be attributed to the known formation of oligomers for aluminum phenoxides. It is worth noting that despite its ill-defined nature, the isolated material has the same performance in the hydroboration of 2-acethylpyridine as *in situ* formed [(R)-CF_3-BINOL-AlMe]$_2$, giving 98% conversion with 97% ee at 1 mol % loading.

Thus, we assumed that a more sterically hindered substrate can provide a monomeric, well defined adduct. Upon addition of 1 equiv. of [(R)-CF_3-BINOL-AlMe]$_2$ to an *n*-hexane solution of (4-fluorophenyl)(2-pyridinyl) methanone (**1k**, 3 equiv.) a grayish precipitate was formed. Upon filtration and according to the mass balance, a 1:1 adduct **4** was formed (Scheme 1). The complex was characterized by liquid state ^{1}H, ^{13}C, ^{19}F NMR and solid-state IR spectroscopy. The adduct is stable in a solution of benzene-d_6 and in the solid state for several days. Integration of the ^{19}F NMR spectrum shows a 1:12 ratio for the Ph-F and the –CF_3 groups, respectively (SI, Figure S10). The resonance signals of the trifluoromethyl groups appear as two singlets, pointing to a dynamic behavior of the molecule in solution.

In the solid-state IR spectrum (Figure S16 and S12 respectively), the bathochromic shift (ν = 53 cm^{-1}) of the C=O stretching vibration is observed for **4** (ν = 1598 cm^{-1}) compared to the free ketone **1k** (ν = 1651 cm^{-1}). The Al-Me resonances in ^{1}H and ^{13}C NMR spectra of **4** shift to downfield

δ = −0.94/−11.7 ppm compared to those in the starting material δ = −1.32/−16.4 ppm (SI, Figures S10 and S9, respectively). Previously reported data for $AlMe(BHT)_2$ (BHT = 2,6-di-*tert*-butyl-4-methylphenolate) adducts with a number of diaryl, aryl-alkyl and dialkyl ketones show that Al-Me resonance peaks in ^{1}H and ^{13}C NMR spectra also undergo similar downfield shifts upon complexation.[13] However, the bathochromic shifts of the carbonyl stretching vibrations is significantly stronger (ca. 100 – 115 cm^{-1}), which is presumably due to the coordination number at the Al center.

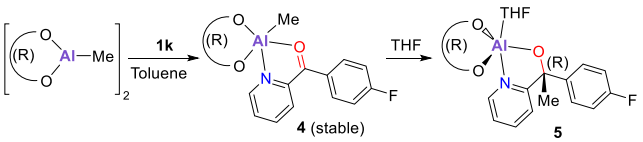

Scheme 1. Reactivity of [(R)-CF_3-BINOL-AlMe]$_2$ towards (4-fluorophenyl)(2-pyridinyl)methanone (**1k**).

Upon dissolving **4** in THF-d_8, the Al-Me signal disappears in the ^{1}H and ^{13}C NMR spectra and a singlet corresponding to the Me group appears at δ = 1.42 and 32.58 ppm, respectively. Only one set of signals was observed in ^{1}H, ^{13}C and ^{19}F NMR spectra pointing to highly stereoselective methyl transfer. The reaction was repeated on a preparative scale and five-coordinate aluminum complex **5** was isolated in 60% yield after crystallization. This compound was spectroscopically and structurally characterized (Scheme 1, Figure 4).

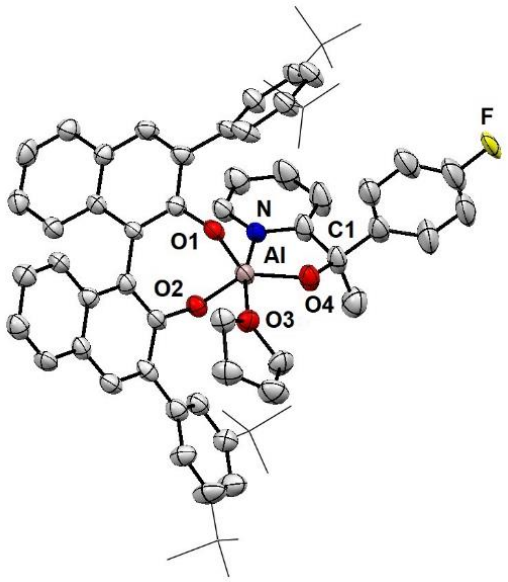

Figure 4. MERCURY plot of the molecular structure of **5**. Hydrogen atoms are omitted for clarity. Selected bond lengths [Å] and angles [°]: Al-O1 1.764(5), Al-O2 1.792(6), Al-O3 1.967(6), Al-O4 1.764(7), Al-N 2.065(7). O1-Al-O2 104.5(3), O1-Al-O4 121.8(3), O1-Al-O3 92.0(2), O1-Al-N 99.7(3), O2-Al-O4 133.7(3), O2-Al-N 89.4(3), O3-Al-O4 85.8(3), O3-Al-N 166.6(3), O4-Al-N 82.5(3).

The broad signals in the ^{1}H and ^{13}C NMR spectra for the THF ligand and a sharp singlet for all $-CF_3$ groups indicate a fluctuating coordination environment at the aluminum center. The central atom in **5** adopts a distorted trigonal bipyramidal coordination geometry with the THF and pyridine ligands occupying axial positions (Figure 4). In an NMR experiment, where 2-acetylpyridine (**1a**) was added directly to a solution of [(R)-BINOL-AlMe(THF)$_2$]$_2$ in THF-d_8 no reaction was observed at ambient temperature (SI, Figures S7 and S8), demonstrating the importance of the solvent coordinating ability.

Computational Study

To get further insight into the reaction mechanism and the origin of enantioselectivity we have performed DFT calculations, which suggest that the active catalyst is generated *in situ*, as described in Figure 5. The overall catalytic reaction pathway is displayed in Figure 6. In these calculations we considered the complex based on the (*R*)-CF_3-BINOL ligand.

Catalyst Activation: In agreement with the experiments, calculations revealed that the dimeric form of the [(*R*)-CF_3-BINOL-AlMe]$_2$ complex (**C$_1$**) is more stable compared to the monomeric form by 19.9 kcal/mol. We thus considered the dimeric species **C$_1$** as starting point of the activation pathway shown in Figure 5. Coordination of two molecules of 2-acetylpyridine (**1a**) converts the dimeric species **C$_1$** to two monomeric species **C$_2$** by an exergonic step of 3.1 kcal/mol per **C$_2$** molecule. Coordination of a second molecule of **1a** to **C$_2$** facilitates the migration of the –Me group from aluminum to the carbonyl group via transition state [**C$_3$**-**C$_4$**]‡ and an activation barrier of 24.3 kcal/mol from **C$_2$**, leading to **C$_4$**. In the absence of the second **1a** molecule the activation barrier for the migration of the –Me group to Al in **C$_2$** amounts to 31.4 kcal/mol (see Figure S1). An indirect experimental proof that an additional ligand facilitates the migration of the Me group is the conversion of **4** to **5** upon dissolving **4** in THF-d_8 (Scheme 1).

The resulting intermediate **C$_4$** (36.7 kcal/mol below the reactant) can evolve by σ-bond metathesis between the Al–O and H–BPin bonds. The most favorable reaction pathway (see Figure S1 for an unfavored pathway) involves the endergonic dissociation of **1a** from **C$_4$** with almost thermoneutral coordination of HBPin to the Al–O bond, leading to intermediate **C$_6$**. Subsequent, σ-bond metathesis between the Al–O and H–BPin bonds occurs via transition state [**C$_6$**-**C$_7$**]‡ with an energy barrier of 16.1 kcal/mol from **C$_4$**. The resulting Al–H intermediate **C$_7$**, is 10.5 kcal/mol higher in energy compared to the most stable intermediate **C$_4$**. Finally, the Al–H species **A**, generated by coordination of **1a** to **C$_7$** with release of **C$_8$**, is considered as the active catalyst for the hydroboration reaction discussed in the next section.

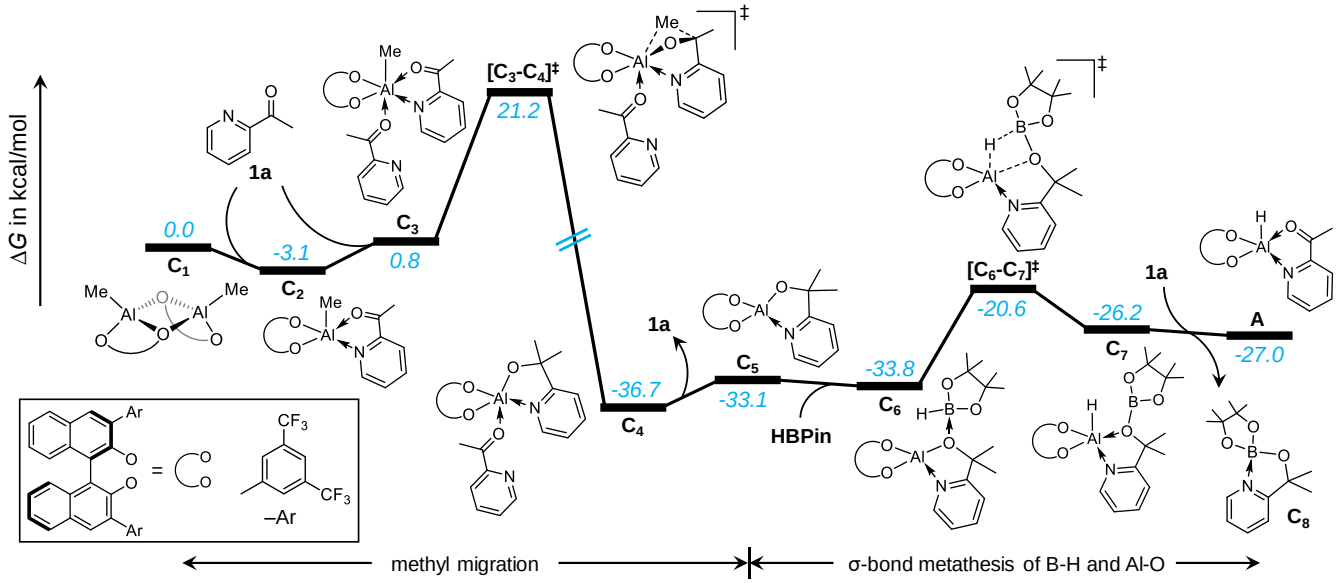

Figure 5. Energy profile for the formation of the active catalyst. Free energies in solution (in kcal/mol) are calculated at the M06/TZVP//BP86/SVP level.

Catalytic Mechanism: The overall catalytic pathway is strictly related to the activation pathway of Figure 5, with the difference that a H-atom (instead of a Me group) migrates to the aluminum atom. For this reason, the catalytic pathway can be divided into two sections: i) hydride migration and ii) σ-bond metathesis between B–H and Al–O bonds. The energy profile and the respective discussion refer to formation of the favored *R* product (*R*)-**2a** (Figure 6). Similarly to the Me migration step during catalyst activation, coordination of a second molecule of **1a** to the aluminum center of **A**, leading to $\mathbf{B_R}$, facilitates hydride migration via the four-membered transition state $[\mathbf{B_R}\text{-}\mathbf{C_R}]^{\ddagger}$ and a moderate energy barrier of 18.2 kcal/mol from **A** + **1a** (see Figure S2 for hydride transfer prior to coordination of a second **1a** molecule). The overall step $\mathbf{B_R}\rightarrow\mathbf{C_R}$ is exergonic by 34.2 kcal/mol. The catalytic cycle evolves further by σ-bond metathesis between the Al–O and the H–BPin bonds. This step starts with dissociation of **1a** from $\mathbf{C_R}$ and coordination of HBPin to the Al-O bond, leading to intermediate $\mathbf{E_R}$, which is 2.1 kcal/mol lower in energy than $\mathbf{D_R}$. No transition state has been located for HBPin coordination to $\mathbf{D_R}$, which is in agreement with previous reports.[14] σ-bond metathesis between the H–BPin and Al–O bonds via transition state $[\mathbf{E_R}\text{-}\mathbf{F_R}]^{\ddagger}$ and an activation barrier of 15.8 kcal/mol from $\mathbf{E_R}$ results in the formation of the Al–H species $\mathbf{F_R}$. Coordination of a **1a** molecule to $\mathbf{F_R}$ releases product (*R*)-**2a** and regenerate the starting catalytic species **A**.

The reaction profile in Figure 6 reveals that hydride migration via transition state $[\mathbf{B_R}\text{-}\mathbf{C_R}]^{\ddagger}$ is the rate-controlling step. Therefore, to rationalize the observed enantio-selectivity we have investigated the hydride migration step towards formation of the opposite enantiomer (*S*)-**2a** (red line in Figure 6, complete energy profile in Figure S3). In agreement with the experimentally observed selectivity, transition state $[\mathbf{B_R}\text{-}\mathbf{C_R}]^{\ddagger}$, leading to formation of (*R*)-**2a**, is favored by 3.7 kcal/mol compared to transition state $[\mathbf{B_S}\text{-}\mathbf{C_S}]^{\ddagger}$, leading to formation of (*S*)-**2a** (for complete pathway refer Figure S3 in SI).

To understand the origin of enantioselectivity we performed an energy decomposition analysis (EDA) of the relative stability of transition states $[\mathbf{B_R}\text{-}\mathbf{C_R}]^{\ddagger}$ and $[\mathbf{B_S}\text{-}\mathbf{C_S}]^{\ddagger}$ (for details refer to Table S6 in SI).[15] Within the EDA the energy difference between transition states $[\mathbf{B_S}\text{-}\mathbf{C_S}]^{\ddagger}$ and $[\mathbf{B_R}\text{-}\mathbf{C_R}]^{\ddagger}$ ($\Delta E^{\ddagger}$) can be decomposed as $\Delta E^{\ddagger} = \Delta E_{def} + \Delta E_{int}$, where ΔE_{def} is the difference between the energies required to deform **A** + **1a** to the geometry of transition states $[\mathbf{B_R}\text{-}\mathbf{C_R}]^{\ddagger}$ and $[\mathbf{B_S}\text{-}\mathbf{C_S}]^{\ddagger}$, and ΔE_{int} is the difference between the interaction energies of the deformed **A** and **1a** fragments in transition states $[\mathbf{B_R}\text{-}\mathbf{C_R}]^{\ddagger}$ and $[\mathbf{B_S}\text{-}\mathbf{C_S}]^{\ddagger}$ (see Scheme 2).

Scheme 2. Cartoon representation of the scheme used to decompose the activation barrier, $E^{\ddagger}$, into a deformation term, E_{def}, and an interaction term, E_{int}.

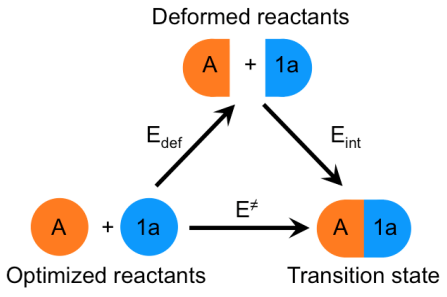

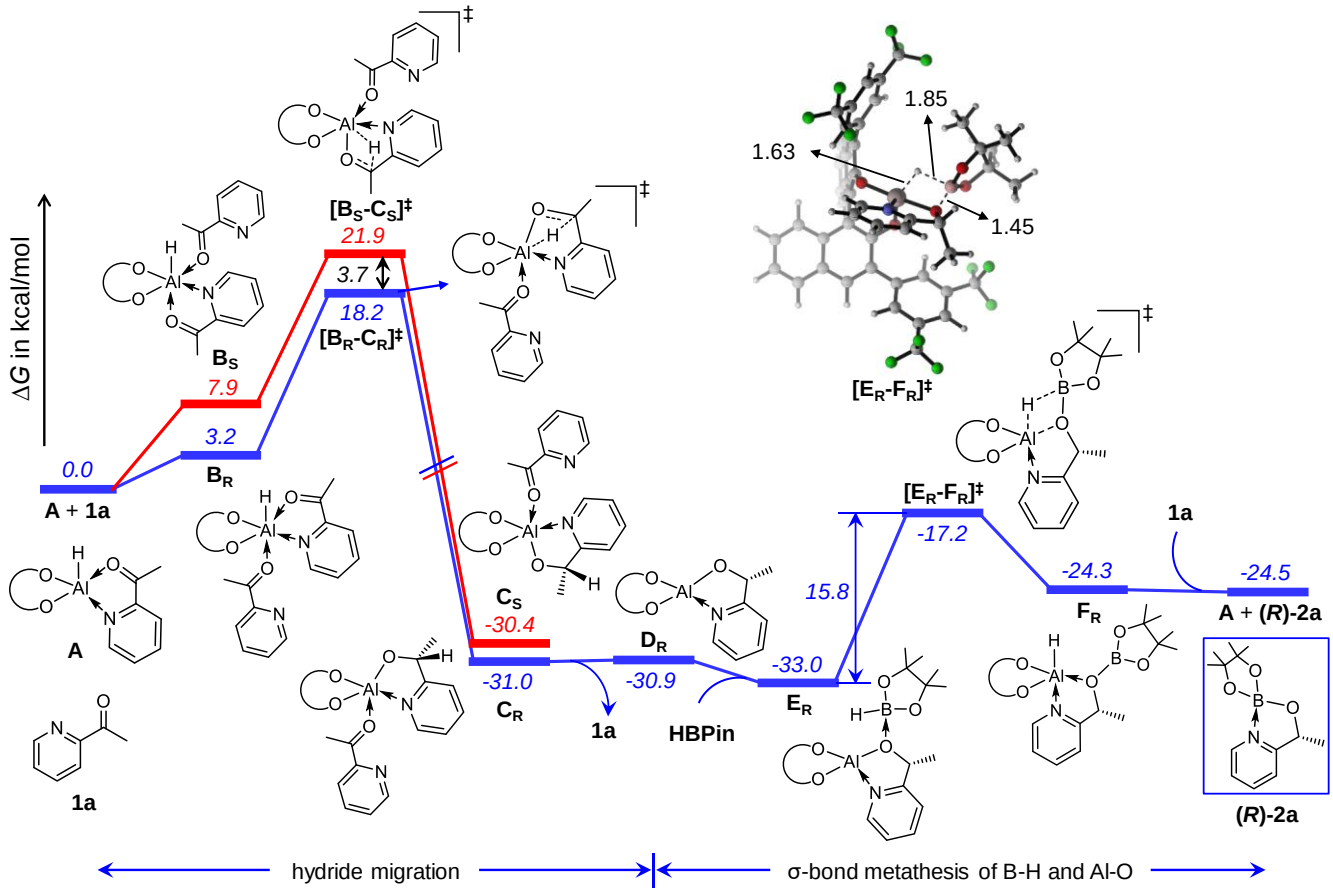

Figure 6. Energy profile for the catalytic reaction. Blue line for selective (*R*)-2a product formation pathway and red line for rate limiting step towards (*S*)-2a product. Bond lengths are in Å. Free energies in solution (in kcal/mol) at the M06/TZVP//BP86/SVP level are displayed.

Calculations reveal that the higher stability of transition state **[B$_R$-C$_R$]**‡, $\Delta E^{\ddagger}$ = 3.4 kcal/mol, is due to the smaller energy required to deform **A** + **1a** to the geometry of transition state **[B$_R$-C$_R$]**‡, rather than to that of transition state **[B$_S$-C$_S$]**‡, for a ΔE_{def} = 10.7 kcal/mol. The positive ΔE_{def} favoring **[B$_R$-C$_R$]**‡ is not compensated by the higher interaction energy between **A** and **1a** in transition states **[B$_S$-C$_S$]**‡, for a ΔE_{int} = -7.3 kcal/mol. This suggests that transition state **[B$_S$-C$_S$]**‡ is destabilized by steric repulsion between **A** and **1a**.

Inspection of the geometries of transition states **[B$_R$-C$_R$]**‡ and **[B$_S$-C$_S$]**‡ (see Figure 7) shows that the reacting groups and the ancillary **1a** molecule in **[B$_R$-C$_R$]**‡ are placed away from the (*R*)-CF$_3$-BINOL ligand, while in **[B$_S$-C$_S$]**‡ the aromatic ring of the reacting **1a** molecule and the methyl group of the ancillary **1a** molecule, highlighted in yellow, are at short (repulsive) distances from a CF3 substituted ring and the binaphthol skeleton of the (*R*)-CF$_3$-BINOL ligand, respectively. The repulsive interaction involving the binaphthol skeleton explain the relatively high *ee* observed in presence of the (*R*)-BINOL ligand (see Table 1), despite it has no ortho substituents.

As the above analyses indicated that the main parameter impacting enantioselectivity can be related to repulsive interactions in the pro-(*S*) transition state, due to clashes between the reacting group and the (*R*)-CF$_3$-BINOL ligand, to rationalize the performance of the whole set of 6 catalysts used experimentally we analyzed their steric properties. To this end we analyzed the optimized geometry of intermediate **A** for the 6 ligands reported in Table 1 using the buried volume family of descriptors.[16] Plotting both the conversion and the *ee* versus the %V$_{Bur}$ results in a volcano plot, with highest conversion and enantio-selectivity in the %V$_{Bur}$ range of 34-38% (Figure 8a). Further increase of steric hindrance results in declining performances, see the trend from (*R*)-CF$_3$-BINOL to (*R*)-TADDOL and to (*R*)-SiPh$_3$-BINOL. Comparison of the steric maps of these complexes (Figure 8b-c) shows the impact of the ligand skeleton on the catalytic pocket around the aluminum center.

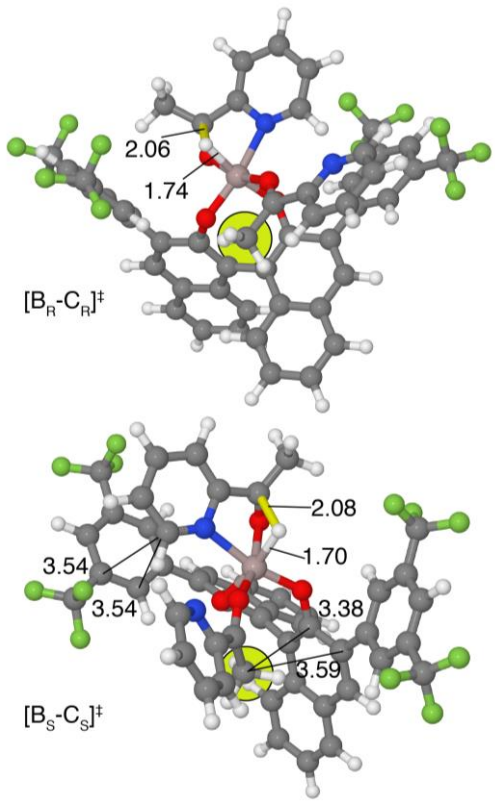

Figure 7. Optimized geometries of transition states for hydride migration step. Bond lengths are in Å. The emerging C–H bond is colored in yellow. The methyl group of the ancillary **1a** molecule is highlighted in yellow.

Compared to (*R*)-BINOL, the catalytic pocket of (*R*)-CF_3-BINOL shows increasing steric hindrance around the north-west and south-east borders, while the catalytic pocket of (*R*)-$SiPh_3$-BINOL is clearly more hindered than that of (*R*)-CF_3-BINOL. These insights offer an explanation for the lower performance of the (*R*)-BINOL and (*R*)-$SiPh_3$-BINOL complexes. Specifically, the low steric hindrance in (*R*)-BINOL suggests it can results in a very stable dimeric aluminum complex $\mathbf{C_1}$. We thus calculated the energy for the opening of $\mathbf{C_1}$ by **1a** to give the monomeric complex $\mathbf{C_2}$ (see Figure 5), and we found that in presence of the (*R*)-BINOL ligand this process is disfavored by 4.4 kcal/mol. In contrast, opening of the dimeric complex $\mathbf{C_1}$ with (*R*)-CF_3-BINOL is favored by 3.1 kcal/mol (see Figure 5). The high stability of the dimeric aluminum complex with the (*R*)-BINOL ligand explains the experimentally observed reduced conversion promoted by this ligand (see Table 1). As for (*R*)-$SiPh_3$-BINOL, its high steric hindrance suggests it can disfavor coordination of two **1a** molecules to the aluminum center, needed to promote migration of both the –Me group and the –H atom. We thus calculated the energy for coordinating a **1a** molecule to $\mathbf{C_2}$ to give complex $\mathbf{C_3}$ (see Figure 5), and we found that in presence of the (*R*)-$SiPh_3$-BINOL ligand this process is disfavored by 10.9 kcal/mol. In contrast, coordination of **1a** to $\mathbf{C_2}$ with (*R*)-CF_3-BINOL is disfavored by 3.9 kcal/mol only (see Figure 5). The more difficult coordination of the second **1a** molecule with the (*R*)-$SiPh_3$-BINOL ligand explains the experimentally observed reduced conversion promoted by this ligand (see Table 1).

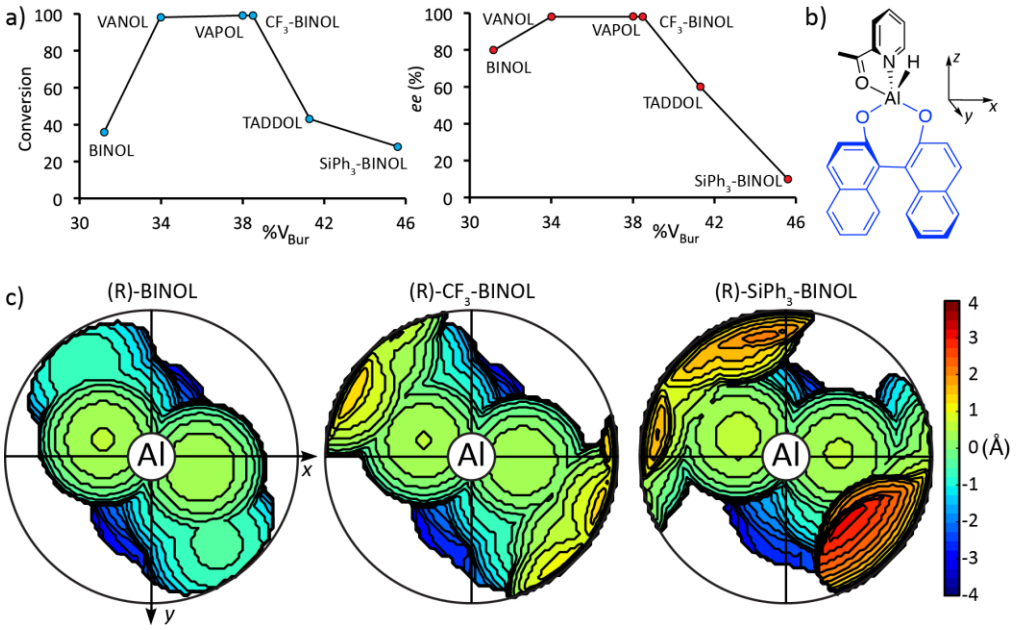

Figure 8. Part a, plots of the experimental conversion and *ee* versus the buried volume of the 6 binapthol ligands in the optimized geometry of complex **A**. Part b), orientation of the **A** complex in the cartesian frame used to calculated the buried volume and the steric maps. Part c), steric map of the (*R*)- BINOL, (*R*)-CF_3-BINOL and (*R*)-$SiPh_3$-BINOL ligands in the optimized geometry of complex **A**.

CONCLUSIONS

In summary, we have developed a versatile protocol for a highly enantioselective hydroboration of 2-pyridine and similar heterocyclic ketones utilizing an *in situ* formed aluminum complex bearing readily available VANOL, VAPOL and BINOL based ligands. The ligand can be fully recovered and reused. Short reaction times, as well as broad scope of substrates make this protocol a valuable synthetic tool in organic synthesis. The catalyst was isolated and structurally as well as spectroscopically characterized. Several intermediates which provide insight into the catalytic cycle were spectroscopically or/and structurally identified. A detailed reaction mechanism fully confirming our empirical observations is proposed based on computational studies. Steric analysis indicated that top performances can only be achieved if appropriate tuning of the steric hindrance around the active center is performed.

ASSOCIATED CONTENT

Supporting Information. This material is available free of charge on the ACS Publication Website at DOI:
NMR and IR Spectra, HPLC traces and Computational Details (PDF)
X-Ray crystallographic data (CIF)

AUTHOR INFORMATION

Corresponding Authors

* magnus.rueping@rwth-aachen.de
* yury.lebedev@kaust.edu.sa
* luigi.cavallo@kaust.edu.sa
* bholanath.maity@kaust.edu.sa

Author Contributions

The manuscript was written through contributions of all authors. / All authors have given approval to the final version of the manuscript.

ACKNOWLEDGMENT

B.M. and L.C. acknowledge King Abdullah University of Science and Technology (KAUST) for support and the KAUST Supercomputing Laboratory for providing computational resources of the supercomputer Shaheen II.
Miguel Dinis Veloso Guerreiro (KAUST) is acknowledged for providing several starting materials.

REFERENCES

(1) (a) Weber, R. W.; Nelson, H. S. Pirbuterol Hydrochloride: Evaluation of Beta Adrenergic Agonist Activity in Reversible Obstructive Pulmonary Disease and Congestive Heart Failure. *Pharmacother. J. Hum. Pharmacol. Drug Ther.* **1984**, *4*, 1–9. (b) Meguro, K.; Aizawa, M.; Sohda, T.; Kawamatsu, Y.; Nagaoka, A. New 1,4-Dihydropyridine Derivatives with Potent and Long-Lasting Hypotensive Effect. *Chem. Pharm. Bull.* **1985**, *33*, 3787–3797. (c) Casy, A. F.; Drake, A. F.; Ganellin, C. R.; Mercer, A. D.; Upton, C. Stereochemical Studies of Chiral H-1 Antagonists of Histamine: The Resolution, Chiral Analysis, and Biological Evaluation of Four Antipodal Pairs. *Chirality* **1992**, *4*, 356–366. (d) Botta, M.; Summa, V.; Corelli, F.; Di Pietro, G.; Lombardi, P. Synthesis of Aryl 2-Benzofuranyl and Aryl 2-Indolyl Carbinols of High Enantiomeric Purity via Palladium-Catalyzed Heteroannulation of Chiral Arylpropargylic Alcohols. *Tetrahedron: Asymmetry* **1996**, *7*, 1263–1266. (e) Farina, V.; Reeves, J. T.; Senanayake, C. H.; Song, J. J. Asymmetric Synthesis of Active Pharmaceutical Ingredients. *Chem. Rev.* **2006**, *106*, 2734–2793. (f) Yoshizumi, T.; Takahashi, H.; Miyazoe, H.; Sugimoto, Y.; Tsujita, T.; Kato, T.; Ito, H.; Kawamoto, H.; Hirayama, M.; Ichikawa, D.; Azuma-Kanoh, T.; Ozaki, S.; Shibata, Y.; Tani, T.; Chiba, M.; Ishii, Y.; Okuda, S.; Tadano, K.; Fukuroda, T.; Okamoto, O.; Ohta, H. A Novel Class of Cycloalkano[b]Pyridines as Potent and Orally Active Opioid Receptor-like 1 Antagonists with Minimal Binding Affinity to the HERG K+ Channel. *J. Med. Chem.* **2008**, *51*, 4021–4029. (g) Leahy, D. K.; Fan, Y.; Desai, L. V.; Chan, C.; Zhu, J.; Luo, G.; Chen, L.; Hanson, R. L.; Sugiyama, M.; Rosner, T.; Cuniere, N.; Guo, Z.; Hsiao, Y.; Gao, Q. Efficient and Scalable Enantioselective Synthesis of a CGRP Antagonist. *Org. Lett.* **2012**, *14*, 4938–4941. (h) Sousa, C. A. D.; Sampaio-Dias, I. E.; Rizzo-Aguiar, F.; Garcia-Mera, X.; Rodríguez-Borges, J. E. Enantiopure Synthesis of 7-(1-Pyrindanyl)Propargyl Ethers as Rasagiline Analogues via Chemical or Enzymatic Resolution of 1-Pyrindan-7-Ol. *RSC Adv.* **2015**, *5*, 104509–104515.
(2) (a) Bolm, C.; Schlingloff, G.; Harms, K. Catalyzed Enantioselective Alkylation of Aldehydes. *Chem. Ber.* **1992**, *125*, 1191–1203. (b) Telfer, S. G.; Sato, T.; Kuroda, R. Noncovalent Ligand Strands for Transition-Metal Helicates: The Straightforward and Stereoselective Self-Assembly of Dinuclear Double-Stranded Helicates Using Hydrogen Bonding. *Angew. Chem. Int. Ed.* **2004**, *43* (5), 581–584. (c) Telfer, S. G.; Kuroda, R. The Versatile, Efficient, and Stereoselective Self-Assembly of Transition-Metal Helicates by Using Hydrogen-Bonds. *Chem. – Eur. J.* **2005**, *11*, 57–68. (d) Gibson, H. W.; Berg, M. A. G.; Dickson, J. C.; Lecavalier, P. R.; Wang, H.; Merola, J. S. Diastereomeric Reissert Compounds of Isoquinoline and 6,7-Dimethoxy-3,4-Dihydroisoquinoline in Stereoselective Synthesis. *J. Org. Chem.* **2007**, *72*, 5759–5770. (e) Telfer, S. G.; Parker, N. D.; Kuroda, R.; Harada, T.; Lefebvre, J.; Leznoff, D. B. Helicates, Boxes, and Polymers from Simple Pyridine-Alcohol Ligands: The Impact of the Identity of the Transition Metal Ion. *Inorg. Chem.* **2008**, *47*, 209–218. (f) Xie, Y.; Huang, H.; Mo, W.; Fan, X.; Shen, Z.; Shen, Z.; Sun, N.; Hu, B.; Hu, X. Design and Synthesis of New Chiral Pyridine–Phosphite Ligands for the Copper-Catalyzed Enantioselective Conjugate Addition of Diethylzinc to Acyclic Enones. *Tetrahedron Asymmetry* **2009**, *20*, 1425–1432. (g) Woodmansee, D. H.; Müller, M.-A.; Neuburger, M.; Pfaltz, A. Chiral Pyridyl Phosphinites with Large Aryl Substituents as Efficient Ligands for the Asymmetric Iridium-Catalyzed Hydrogenation of Difficult Substrates. *Chem. Sci.* **2010**, *1*, 72–78. (h) Chorazy, S.; Podgajny, R.; Nitek, W.; Fic, T.; Görlich, E.; Rams, M.; Sieklucka, B. Natural and Magnetic Optical Activity of 2-D Chiral Cyanido-Bridged MnII–NbIV Molecular Ferrimagnets. *Chem. Commun.* **2013**, *49*, 6731–6733. (i) DiSalvo, F.; Tsang, M. Y.; Teixidor, F.; Viñas, C.; Planas, J. G.; Crassous, J.; Vanthuyne, N.; Aliaga-Alcalde, N.; Ruiz, E.; Coquerel, G.; Clevers, S.; Dupray, V.; Choquesillo-Lazarte, D.; Light, M. E.; Hursthouse, M. B. A Racemic and Enantiopure Unsymmetric Diiron(III) Complex with a Chiral o-Carborane-Based Pyridylalcohol Ligand: Combined Chiroptical, Magnetic, and Nonlinear Optical Properties. *Chem. – Eur. J.* **2014**, *20*, 1081–1090. (j) Carmona, D.; Lamata, P.; Sánchez, A.; Pardo, P.; Rodríguez, R.; Ramírez, P.; Lahoz, F. J.; García-Orduña, P.; Oro, L. A. Hydroxymethylpyridine Containing Half-Sandwich Complexes of Rh(III), Ir(III) or Ru(II). *Dalton Trans.* **2014**, *43*, 15546–15559. (k) Horeglad, P.; Cybularczyk, M.; Litwińska, A.; Dąbrowska, A. M.;

Dranka, M.; Żukowska, G. Z.; Urbańczyk, M.; Michalak, M. Controlling the Stereoselectivity of Rac-LA Polymerization by Chiral Recognition Induced the Formation of Homochiral Dimeric Metal Alkoxides. *Polym. Chem.* **2016**, *7*, 2022–2036. (l) Schumacher, A.; Bernasconi, M.; Pfaltz, A. Chiral N-Heterocyclic Carbene/Pyridine Ligands for the Iridium-Catalyzed Asymmetric Hydrogenation of Olefins. *Angew. Chem. Int. Ed.* **2013**, *52*, 7422–7425.

(3) Simons, F. E. R.; Simons, K. J. Histamine and H1-antihistamines: Celebrating a century of progress. *J. Allergy Clin. Immunol.* **2011**, *128*, 1139–1150.

(4) (a) Shin, C.; Okabe, A.; Ito, A.; Ito, A.; Yonezawa, Y. Novel Synthesis of the Main Central 2,3,6-Trisubstituted Pyridine Skeleton [Fragment A-B-C] of a Macrobicyclic Antibiotic, Cyclothiazomycin. *Bull. Chem. Soc. Jpn*. **2002**, *75*, 1583–1596.

(b) Uenishi, J.; Hamada, M.; Aburatani, S.; Matsui, K.; Yonemitsu, O.; Tsukube, H. Synthesis of Chiral Nonracemic 1-(2-Pyridinyl)Ethylamines: Stereospecific Introduction of Amino Function onto the 2-Pyridinylmethyl Carbon Center. *J. Org. Chem.* **2004**, *69*, 6781–6789.

(c) Uenishi, J.; Hamada, M. Synthesis of Enantiomerically Pure 8-Substituted 5,6,7,8-Tetrahydroquinolines. *Synthesis*, **2002**, *5*, 0625–0630.

(5) Truppo, M. D.; Pollard, D.; Devine, P. Enzyme-Catalyzed Enantioselective Diaryl Ketone Reductions. *Org. Lett.* **2007**, *9*, 335–338.

(6) Corey, E. J.; Helal, C. J. Asymmetric Synthesis of (S)-Carbinoxamine. New Aspects of Oxazaborolidine-Catalyzed Enantioselective Carbonyl Reduction. *Tetrahedron Lett.* **1996**, *37*, 5675–5678.

(7) (a) Ohkuma, T.; Koizumi, M.; Yoshida, M.; Noyori, R. General Asymmetric Hydrogenation of Hetero-Aromatic Ketones. *Org. Lett.* **2000**, *2*, 1749–1751. (b) Lee, C.-T.; Lipshutz, B. H. Nonracemic Diarylmethanols From CuH-Catalyzed Hydrosilylation of Diaryl Ketones. *Org. Lett.* **2008**, *10*, 4187–4190. (c) Tao, X.; Li, W.; Ma, X.; Li, X.; Fan, W.; Xie, X.; Ayad, T.; Ratovelomanana-Vidal, V.; Zhang, Z. Ruthenium-Catalyzed Enantioselective Hydrogenation of Aryl-Pyridyl Ketones. *J. Org. Chem.* **2012**, *77*, 612–616. (d) Yang, H.; Huo, N.; Yang, P.; Pei, H.; Lv, H.; Zhang, X. Rhodium Catalyzed Asymmetric Hydrogenation of 2-Pyridine Ketones. *Org. Lett.* **2015**, *17*, 4144–4147. (e) Wang, B.; Zhou, H.; Lu, G.; Liu, Q.; Jiang, X. Bifunctional Oxo-Tethered Ruthenium Complex Catalyzed Asymmetric Transfer Hydrogenation of Aryl N-Heteroaryl Ketones. *Org. Lett.* **2017**, *19*, 2094–2097. (f) Zheng, L.-S.; Llopis, Q.; Echeverria, P.-G.; Férard, C.; Guillamot, G.; Phansavath, P.; Ratovelomanana-Vidal, V. Asymmetric Transfer Hydrogenation of (Hetero)Arylketones with Tethered Rh(III)–N-(p-Tolylsulfonyl)-1,2-Diphenylethylene-1,2-Diamine Complexes: Scope and Limitations. *J. Org. Chem.* **2017**, *82*, 5607–5615. (g) Liu, Q.; Wang, C.; Zhou, H.; Wang, B.; Lv, J.; Cao, L.; Fu, Y. Iridium-Catalyzed Highly Enantioselective Transfer Hydrogenation of Aryl *N*-Heteroaryl Ketones with *N*-Oxide as a Removable Ortho-Substituent. *Org. Lett.* **2018**, *20*, 971–974.

(8) (a) Stephan, D. W.; Erker, G. Frustrated Lewis Pair Chemistry: Development and Perspectives. *Angew. Chem*. **2015**, *54*, 2 – 44. (b) Wilkins, L. C.; Melen, R. L. Enantioselective Main Group Catalysis: Modern Catalysts for Organic Transformations. *Coord. Chem. Rev*. **2016**, *324*, 123 – 139. (c) Adams, M. R; Tien, C.-H.; McDonald, R.; Speed, A. W. H. Asymmetric Imine Hydroboration Catalyzed by Chiral Diazaphospholenes. *Angew. Chem*. **2017**, *56*, 16660 – 16663.

(9) (a) Li, W.; Ma, X.; Walawalkar, M. G.; Yang, Z.; Roesky, H. W. Soluble Aluminum Hydrides Function as Catalysts in Deprotonation, Insertion, and Activation Reactions. *Coord. Chem. Rev.* **2017**, *350*, 14–29. (b) Yang, Z.; Zhong, M.; Ma, X.; Nijesh, K.; De, S.; Parameswaran, P.; Roesky, H. W. An Aluminum Dihydride Working as a Catalyst in Hydroboration and Dehydrocoupling. *J. Am. Chem. Soc.* **2016**, *138*, 2548–2551. (c) Yang, Z.; Zhong, M.; Ma, X.; De, S.; Anusha, C.; Parameswaran, P.; Roesky, H. W. An Aluminum Hydride That Functions like a Transition-Metal Catalyst. *Angew. Chem. Int. Ed.* **2015**, *54*, 10225–10229. (d) Nikonov, G. I. New Tricks for an Old Dog: Aluminum Compounds as Catalysts in Reduction Chemistry. *ACS. Catal*. **2017**, *7*, 7257–7266. (e) Zhang, G.; Wu, J.; Zeng, H.; Neary, C. M.; Devany, M.; Zheng. S.; Dub, A. P. Dearomatization and Functionalization of Terpyridine Ligands Leading to Unprecedented Zwitterionic Meisenheimer Aluminum Complexes and Their Use in Catalytic Hydroboration. *ACS. Catal*. **2019**, *9*, 874–884.

f) Nikonov, G. I. New Tricks for an Old Dog: Aluminum Compounds as Catalysts in Reduction Chemistry. *ACS. Catal*. **2017**, *7*, 7257–7266.

(10) (a) Pollard, V. A.; Orr, S. A.; McLellan, R.; Kennedy, A. R.; Hevia, E.; Mulvey, R. E. Lithium Diamidodihydridoaluminates: Bimetallic Cooperativity in Catalytic Hydroboration and Metallation Applications. *Chem. Commun.* **2018**, *54*, 1233–1236. (b) Jakhar, V. K.; Barman, M. K.; Nembenna, S. Aluminum Monohydride Catalyzed Selective Hydroboration of Carbonyl Compounds. *Org. Lett.* **2016**, *18*, 4710–4713.

(11) Pyykkö, P.; Atsumi, M. Molecular Double-Bond Covalent Radii for Elements Li–E112. *Chem. Eur. J.* **2009**, *15*, 12770–12779.

(12) (a) Yasuda, M.; Yoshioka, S.; Nakajima, H.; Chiba, K.; Baba, A. Fine-Tuning of Boron Complexes with Cage-Shaped Ligand Geometry: Rational Design of Triphenolic Ligand as a Template for Structure Control. *Org. Lett.* **2008**, *10*, 929–932. (b) Nakajima, H.; Yasuda, M.; Takeda, R.; Baba, A. Recognition of Aromatic Compounds by π Pocket within a Cage-Shaped Borate Catalyst. *Angew. Chem. Int. Ed.* **2012**, *51*, 3867–3870.

(13) (a) Power, M. B.; Barron, A. R.; Bott, S. G.; Atwood, J. L. π-Face Selectivity of Coordinated Ketones to Nucleophilic Additions: The Importance of Aluminum-Oxygen π-Bonding. *J. Am. Chem. Soc.* **1990**, *112*, 3446–3451. (b) Power, M. B.; Bott, S. G.; Clark, D. L.; Atwood, J. L.; Barron, A. R. Interaction of Organic Carbonyls with Sterically Crowded Aryloxide Compounds of Aluminum. *Organometallics* **1990**, *9*, 3086–3097.

(14) Prashanth, B.; Bhandari, M.; Ravi, S.; Shamasundar, K. R.; Singh, S. Electronically Unsaturated Three Coordinate Aluminum Hydride and Organoaluminum Cations. *Chem. Eur. J.* **2018**, *24*, 4794–4799.

(15) (a) Morokuma, K. Molecular Orbital Studies of Hydrogen Bonds. III. C=O···H–O Hydrogen Bond in H2CO···H2O and H2CO···2H2O. *J. Chem. Phys*. **1971**, *55*, 1236–1244. (b) Ziegler, T.; Rauk, A. On the calculation of bonding energies by the Hartree Fock Slater method. *Theor. Chim. Acta*. **1977**, *46*, 1–10. (c) Fernandez, I.; Bickelhaupt, F. M. The activation strain model and molecular orbital theory: understanding and designing chemical reactions. *Chem. Soc. Rev*. **2014**, *43*, 4953-4967. (d) Falivene, L.; Kozlov, S. M.; Cavallo, L. Constructing Bridges between Computational Tools in Heterogeneous and Homogeneous Catalysis. *ACS Catal*. **2018**, *8*, 5637-5656.

(16) (a) Poater, A.; Cosenza, B.; Correa, A.; Giudice, S.; Ragone, F.; Scarano, V.; Cavallo, L. SambVca: A Web Application for the Calculation of the Buried Volume of N-Heterocyclic Carbene Ligands. *Eur. J. Inorg. Chem*. **2009**, 1759-1766. (b) Falivene, L.; Credendino, R.; Poater, A.; Petta, A.; Serra, L.; Oliva, R.; Scarano, V.; Cavallo, L. SambVca 2. A Web Tool for Analyzing Catalytic Pockets with Topographic Steric Maps. *Organometallics*. **2016**, *35*, 2286-2293. (c) Falivene, L.; Cao, Z.; Petta, A.; Serra, L.; Poater, A.; Oliva, R.; Scarano, V.; Cavallo, L. Towards the online computer-aided design of catalytic pockets. *Nat. Chem*. **2019**, *11*, 872-879.

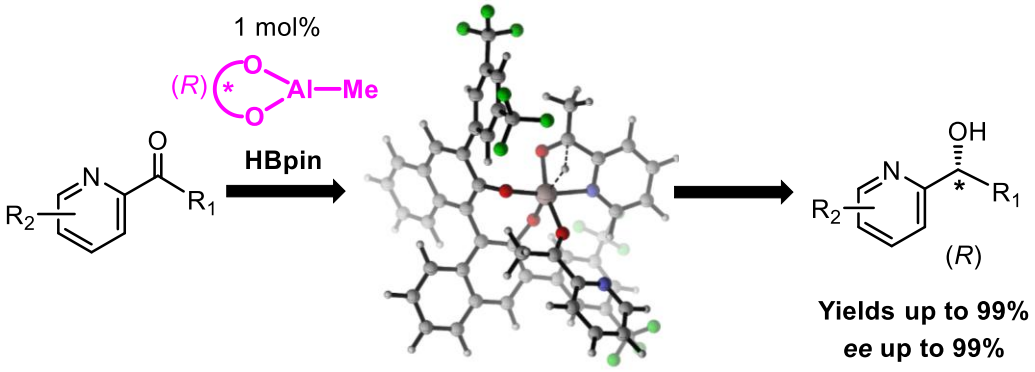
1 mol%
(R)
O
O
Al—Me
HBpin
N
O
R2
R1
OH
N
R2
R1
(R)
Yields up to 99%
ee up to 99%